



Orientation Dependent Twinning Behavior in a Twinning-induced Plasticity Steel Investigated by Nanoindentation

X. K. Shang^{1,2} · S. Pan² · Q. W. Guan² · B. B. He^{1,2,3}

Received: 9 December 2021 / Accepted: 24 January 2022 / Published online: 14 May 2022
© The Korean Institute of Metals and Materials 2022

Abstract

The present work focuses on the mechanical behavior of single austenite grain with different orientations in a twinning induced plasticity (TWIP) steel by nanoindentation test. Deformation twins can be found in [0 0 1]-orientated grains after nanoindentation, while they are absent in grains with [1 1 1] orientation. This inconformity can be ascribed to a larger Schmid factor for leading partial dislocations compared to trailing partial dislocations on the primary slip system in [0 0 1]-orientated grains during compression. Different from deformation twins, high-density dislocations can be found in both [0 0 1] and [1 1 1]-orientated grains after nanoindentation. The present work suggests that the density of deformation twins can be enhanced by controlling crystal orientation through texture engineering or by deformation along different directions such as cross-rolling.

Keywords Deformation twins · Dislocations · High Mn austenitic steel · Nanoindentation

1 Introduction

Strong and ductile steels play key role in designing light-weight structural components in many industries, including automotive and aerospace sectors [1, 2]. The conflict between strength and ductility in steels has been successfully resolved by different strategies, such as transformation induced plasticity (TRIP) effect, twinning induced plasticity (TWIP) effect or the combination of both [3, 4]. The operation of TRIP and TWIP effects can be tuned by controlling the stacking fault energy which is mainly governed by alloying elements such as Mn content [5, 6]. Consequently, based on the amount of Mn element, medium Mn steel and high Mn austenitic steel are classified, with the former dominated by TRIP effect while the latter occupied by TWIP

effect during deformation [7]. High Mn austenitic steel is frequently termed as TWIP steel in the steel community, owing to the contribution of TWIP effect to the excellent combination of strength and ductility [8]. The austenite grains in TWIP steel are decorated with deformation twin boundaries which act as barriers for dislocation slip during the plastic deformation [9]. It is speculated that the effect of deformation twin boundaries in resisting dislocation slip is similar but weaker than that of the high angle grain boundaries [10]. Therefore, the gradual formation of deformation twin boundaries at different strains progressively reduces the dislocation mean free path, demonstrating the dynamic Hall-Patch effect to enhance the work hardening behavior of TWIP steel [11, 12]. Nevertheless, based on detailed synchrotron measurement and analysis, it is found that the contribution of deformation twin boundaries to the flow stress is substantially lower than that of dislocations, suggesting that the TWIP effect on the work hardening behavior of TWIP steel could be overestimated [13]. It is noted that the calculation of overall dislocation density may incorporate the number of dislocations generated due to the presence of deformation twin boundaries. The parallel arrangement of the deformation twin boundaries may be ineffective in inhibiting the dislocation slip as the dislocations can glide along the deformation twin boundaries [14]. In addition to the arrangement of deformation twin boundaries, their amount

✉ B. B. He
hebb@sustech.edu.cn

¹ Shenzhen Key Laboratory of Cross-Scale Manufacturing Mechanics, Southern University of Science and Technology, 518055 Shenzhen, China

² Department of Mechanical and Energy Engineering, Southern University of Science and Technology, 518055 Shenzhen, China

³ Institute for Manufacturing Innovation, Southern University of Science and Technology, 518055 Shenzhen, China

shall also play key role in enhancing the work hardening behavior of TWIP steel.

The existing investigations and drawn conclusions on TWIP steel are mostly based on the macroscopic tensile test [9, 13, 15–21]. However, small-scale test on the single austenite grain of TWIP steel has not been substantially studied [22–25]. The knowledge gained from the small-scale test can shed light on the potential application of TWIP steel in constructing structural components in the nano- and micro-electromechanical system (NEMS/MEMS) [26]. Moreover, such small-scale test can be useful in revealing the deformation mechanisms of individual austenite grains in TWIP steel, complementing the macroscopic mechanical behavior of polycrystalline materials. Small-scale test can be realized through either micro-pillar compression or nanoindentation test. The micro-pillar compression investigation of austenitic pillars in TWIP steel with different diameters reveals a different size effect, that is the critical twinning stress increases with decrease of pillar diameter [25]. The generation of deformation twins depends on the orientation of austenitic pillar in TWIP steel [23]. In addition to the micro-pillar compression test, nanoindentation test is a non-destructive strategy to measure the mechanical behavior of metallic materials at nanoscale [27]. Although nanoindentation test on the medium Mn austenitic steel has been performed [28], such nanoindentation test on high Mn austenitic TWIP steel is seldom reported in the open literature.

The present work investigates the mechanical behavior of single austenite grains in TWIP steel by nanoindentation test. The formation of deformation twins is found to be orientation dependent. In contrast, dislocations can be found in austenite grains with different orientations. The present work suggests that deformation twins are difficult to be generated in certain crystal orientations compared with dislocations. Approaches to enhancing the density of deformation twins are also discussed.

2 Experimental

The nominal chemical composition of the present TWIP steel is Fe-18Mn-0.75 C-1.7Al-0.5Si (wt%). The stacking fault energy of the TWIP steel is estimated to be 29.2 mJ/m² according to the model proposed by Allain [5]. A coarsen-grained austenitic phase without deformation twins is obtained by annealing the prior nanotwinned steel at 1000 °C for 15 min. The nanotwinned steel is processed through 50% reduction cold rolling followed by a recovery annealing at 500 °C for 15 min [29]. Microstructure of the austenite grains in TWIP steel is characterized by Scanning electron microscope (SEM) and electron backscatter diffraction (EBSD) performed on a Zeiss Merlin Field Emission equipment. The step size of EBSD measurement

is either 0.4 or 0.5 μm and the EBSD data is processed by Orientation Imaging Microscopy™ (OIM) software. Nanoindentation tests are carried out in a KLA iNano instrument with a Berkovich indenter in a loading control mode. A constant loading rate up to maximum loads of 1 mN, 3 mN and 5 mN is employed with the loading segment finished in 15 s. Three arrays of indents are made on the austenite grains with different crystal orientation selected by EBSD observation. Distance between two adjacent indent centers is around 8 μm, which is larger than three times of the indentation side length. Thus, the mechanical behaviors of two indentation do not affect each other. The microstructures beneath the indenters after nanoindentation test are characterized by transmission electron microscopy (TEM) in FEI Talos F200X G2. To locate the precise position of indentations and fabricate TEM samples, a focused ion beam (FIB) “lift-out” method is performed in a Helios 600i instrument.

The calculation of Schmid factors is based on the relationship between the applied force on a single crystal and the shear stress on slip plane, which can be expressed as [30, 31]:

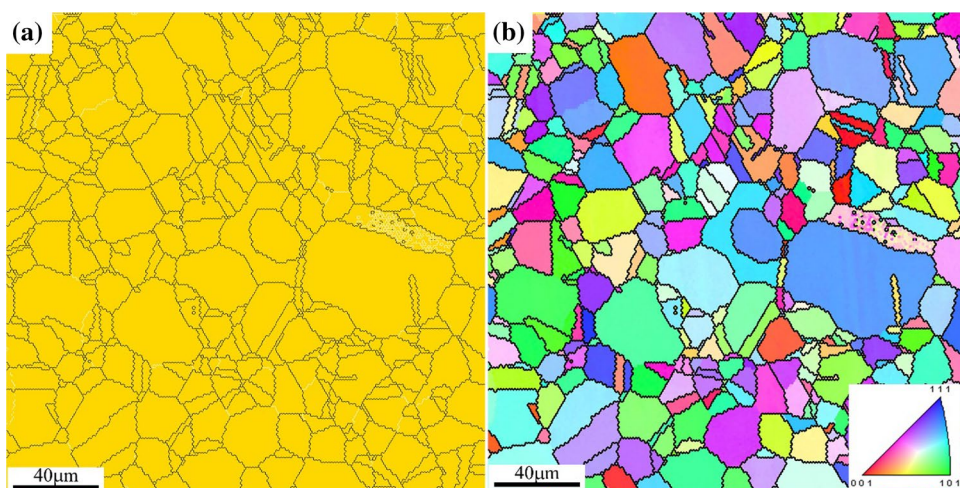
$$\tau = \frac{F}{A} \cos\phi \times \cos\lambda \quad (1)$$

where τ is the resolved shear stress on the slip plane in the slip direction, F is the applied force on the single crystal, A is the cross-sectional area, ϕ is the angle between F and the normal direction to the slip plane, λ is the angle between F and the slip direction. The quantity of $\cos\phi \times \cos\lambda$ is known as the Schmid factor. Accordingly, the Schmid factor values can be calculated by using the Miller indices of the orientations of applied force, slip plane and slip direction. The Schmid factors of $\{1\ 1\ 1\}$ $\langle 1\ 1\ 0\rangle$ primary slip systems, $1/6\ \langle 1\ 1\ 2\rangle$ type Shockley partial dislocations are calculated for each investigated austenitic grain.

3 Results and discussion

The present TWIP steel after annealing at 1000 °C for 15 min demonstrates a single face-center cubic (fcc) austenitic phase as confirmed by the EBSD phase image (Fig. 1a). The average grain size of austenite is estimated to be $16.5 \pm 14.7\ \mu\text{m}$ according to the linear intercept method. The large standard deviation of the grain size could be due to the heterogeneous recrystallization and grain growth during annealing process, which is assisted by prior cold rolling process. Annealing twin boundaries can be frequently detected in the recrystallized austenite

Fig. 1 **a** The EBSD phase map of the present TWIP steel after annealing at 1000 °C for 15 min. Yellow: austenite. **b** The corresponding orientation image of **a**.



grains (Fig. 1b). Generally, the crystal orientation of the austenite grains after high temperature annealing is randomly distributed (Fig. 1b), suggesting it is feasible to perform the nanoindentation test with reliable statistical analysis.

Size and position of the indents after the indentation test are examined by using SEM and EBSD measurements (Fig. 2). Three arrays of 4×10 indentations within the dashed rectangles are shown in Fig. 2a–c, which correspond to maximum loads of 1 mN, 3 mN and 5 mN, respectively. The tiny indents with the maximum load of 1 mN are shown in the SEM image (Fig. 2a) and EBSD image quality map (Fig. 2d). With the increase of indentation load up to 3 mN and 5 mN, the size of indents is more discernible under the similar magnification (Fig. 2a–f). The indents that are close to the annealing twin boundaries and grain boundaries are disregarded for analysis. The corresponding orientations of the austenite grains with indents are shown in Fig. 2g–i. The indents with maximum load of 1 mN are absent in the orientation image because of tiny size (Fig. 2g). In contrast, the indents with maximum load of 3 mN and 5 mN can be identified in the orientation image (Fig. 2h–i). In particular, the indents marked with dashed circles display orientations close to [1 1 1] and [0 0 1], these indents are thus selected for the detailed microstructure observation beneath the indenter.

The load-depth (P - h) curves with a maximum load of 1 mN are shown in Fig. 3a. Pop-ins (or strain bursts) are observed in the curves of both [1 1 1] and [0 0 1]-orientated grains. The magnitude of the pop-ins is 3.17 ± 1.42 nm. The pop-ins become indiscernible with increased maximum load, which may be due to the enlarged scale as compared to the small magnitude of the pop-ins (Fig. 3b and c). The deformation of nanoindentation test consists of elastic and plastic parts and the elastic part can be analyzed by Hertzian elastic solution with a spherical indenter tip [32]:

$$P = \frac{4}{3} E_r R_i^{\frac{1}{2}} h^{\frac{3}{2}} \quad (2)$$

$$\frac{1}{E_r} = \frac{1 - \nu_i^2}{E_i} + \frac{1 - \nu_s^2}{E_s} \quad (3)$$

where P is the applied load, R is the radius of indenter, h is the indentation depth and E_r is the effective indentation modulus. E and ν are the Young's modulus and the Poisson's ratio. The subscript i represents indenter and s denotes specimen. The very early stage of indentation created by Berkovich indenter is assumed as spherical here due to the tip rounding effect. Using the values of $E_i = 1141$ GPa, $\nu_i = 0.07$ [33], $E_s = 169$ GPa, $\nu_s = 0.3$ [29] and $R_i = 50$ nm, the theoretical elastic behavior during indentation can be calculated (dashed lines in Fig. 3a). The maximum shear stress under indentation for elastic deformation can be calculated as [32]:

$$\tau_{max} = 0.31 \sqrt[3]{\frac{6PE_r^2}{\pi^3 R^2}} \quad (4)$$

The average first pop-in load obtained from the P - h curves is 106 μ N. Thus, the maximum shear stress is estimated to be 13.86 GPa, which is much larger than 10% of the shear modulus (~ 65 GPa [29]). Therefore, the first pop-in could be due to the nucleation of dislocations under the tip of indenter [34]. The P - h curve of [0 0 1]-orientated grain exhibits more pop-ins compared with the curve obtained from [1 1 1]-orientated grain (Fig. 3a). This difference could be ascribed to the nucleation of deformation twins in [0 0 1]-orientated grain. It is reported that only the orientations favorable for the generation of Shockley partial dislocations allow the nucleation of deformation twins and the [0 0 1] orientation is favorable for twinning nucleation during compression [23,

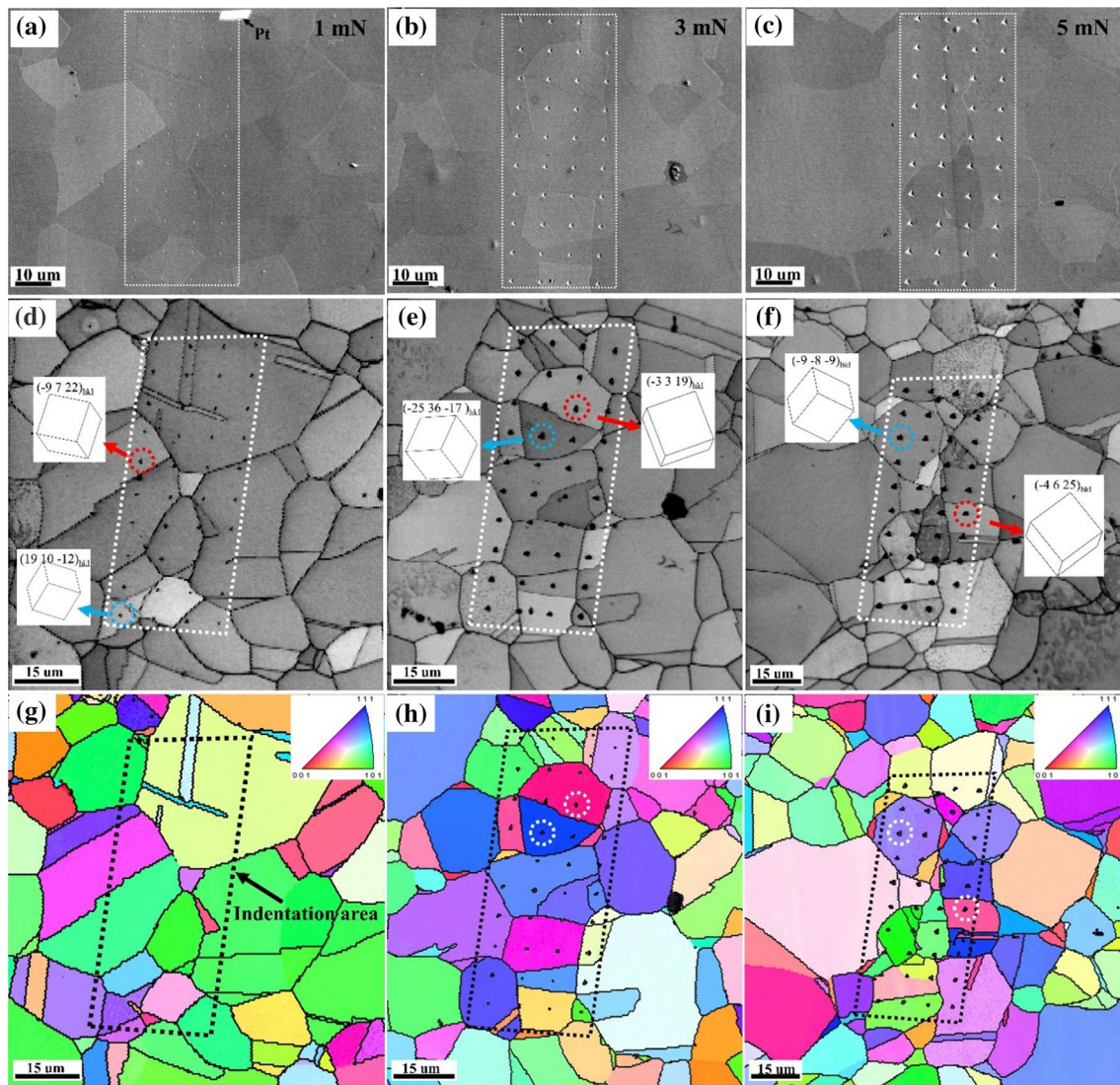


Fig. 2 The SEM image of the present TWIP steel after nanoindentation tests with maximum loads of **a** 1 mN, **b** 3 mN and **c** 5 mN. **d**, **e** and **f** are the corresponding EBSD image quality (IQ) map. The black dots in **d–f** are the indentation impressions. **g–i** are corresponding ori-

entation images of **d–f**, respectively. The dashed circles in **e**, **f**, **h** and **i** mark the position of indents for preparation of TEM samples fabricated by FIB “lift-out” technique. Blue and red colors represent grain orientations close to $[1\ 1\ 1]$ and $[0\ 0\ 1]$, respectively

35]. However, not all the pop-ins should necessarily correspond to the formation of deformation twins, the nucleation of dislocations and the activation of different slip systems should also be considered.

The overall microstructure beneath the indenter in $[1\ 1\ 1]$ -orientated austenite grain under a maximum load of 3 mN is shown in Fig. 4 (a). The dislocations generated by the indentation expand to a depth of around $2\ \mu\text{m}$ (Fig. 4a). The indentation plastic zone is subjected to detailed observation as shown in Fig. 4b and c. No obvious spot for deformation twins can be identified in the selected area diffraction pattern of the indentation plastic zone, suggesting that the deformation twins are not favored in the austenite grain with $[1\ 1\ 1]$ orientation (Fig. 4b). In contrast, profuse dislocations are

detected in the core of indentation plastic zone (Fig. 4c). The straight features in the indentation plastic zone (Fig. 4c) could be ascribed to the formation of perfect dislocations along different slip planes [28].

Figure 5 reveals the formation of defects underneath the indent in a $[0\ 0\ 1]$ -orientated austenite grain under the maximum load of 3 mN. Similar to the indented austenite grain with orientation of $[1\ 1\ 1]$, the travel distance of dislocations is also around $2\ \mu\text{m}$ (Fig. 5a). Striking line feature can be found in the SADP, indicating the formation of stacking faults (Fig. 5a). Interestingly, the magnified view demonstrates the straight features which deserve detailed examination (Fig. 5b). Plentiful dislocations can also be observed in the indentation plastic

Fig. 3 The typical P - h (load-depth) curves of indents with a maximum load of **a** 1 mN, **b** 3 mN and **c** 5 mN, with the orientations of corresponding austenite grains denoted in the upper left insets. Dashed line in **a** is the Hertzian solution curve. Black arrows in **a** indicate the pop-ins of the P - h curves

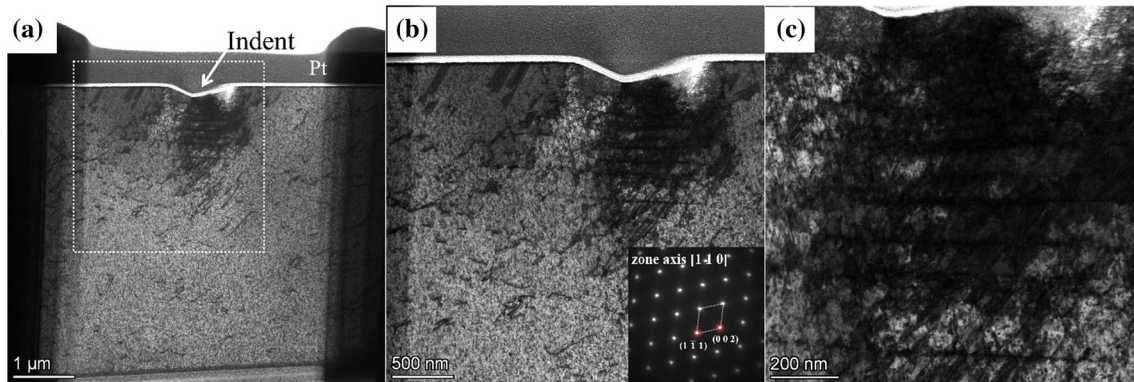
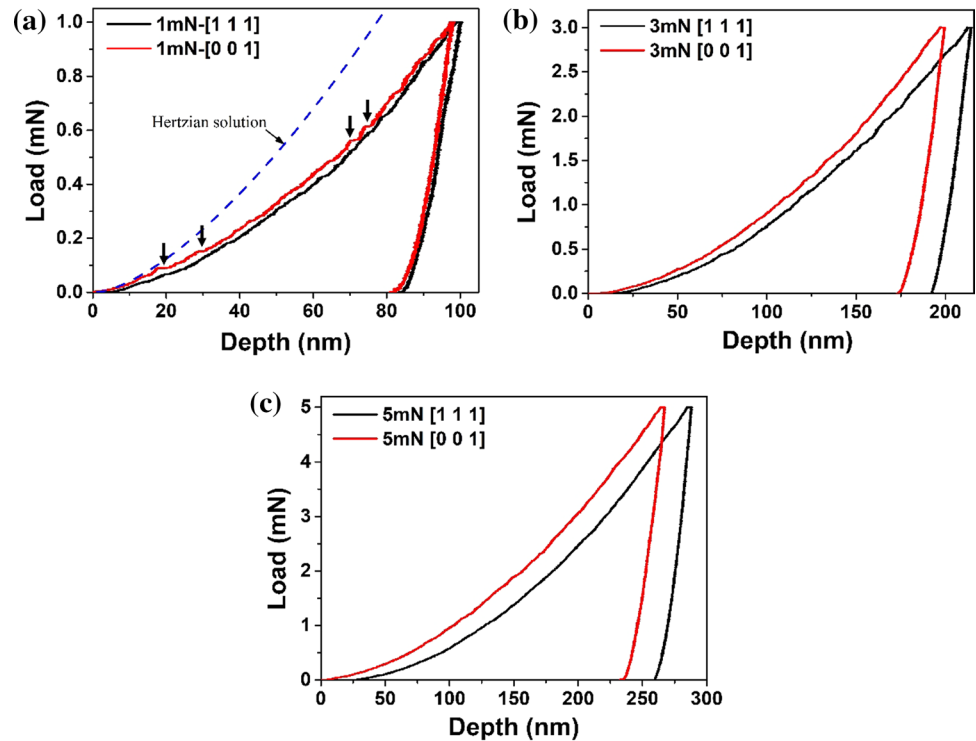


Fig. 4 **a** STEM bright-field image of the microstructure beneath the indent on the austenite grain with orientation of $[1\ 1\ 1]$ under maximum load of 3 mN. **b** The dashed rectangle area of **a**, showing the detailed microstructure under the indent. The lower right inset is

the selected area diffraction pattern (SADP) with a zone-axis of $[1\ 1\ 0]$. **c** The enlarged view of **b** showing the presence of dislocations beneath the indent

zone (Fig. 5c). In addition to the dislocations, lamellar structure is observed within the indentation plastic zone (Fig. 5d). HRTEM image reveals that the lamellar morphology consists of both stacking faults and deformation twins (Fig. 5e, f). Despite the absence of twinning spot in SADP (Fig. 5a), the FFT patterns of HRTEM confirm the formation of deformation twins (Fig. 5e, f). The deformation twins may nucleate beneath the indenter owing to the stress concentration and propagate with increase of indentation load. However, the fraction of deformation twins is much lower compared with stacking faults (Fig. 5e, f).

To further substantiate the absence of deformation twins in the $[1\ 1\ 1]$ -orientated austenite grains, a higher maximum load of 5 mN is applied and the microstructure beneath the indent is examined by TEM observation (Fig. 6a). The travel distance of dislocations is over $4\ \mu\text{m}$, which is larger than that of the dislocations induced by the maximum load of 3 mN (Figs. 4a, 5a). The magnified view confirms the presence of abundant dislocations in the indentation plastic zone, generating a dislocation cell-like structure (Fig. 6b). The cell boundaries consist of entangled dislocations as depicted by the enlarged view (Fig. 6c). The formation of dislocation

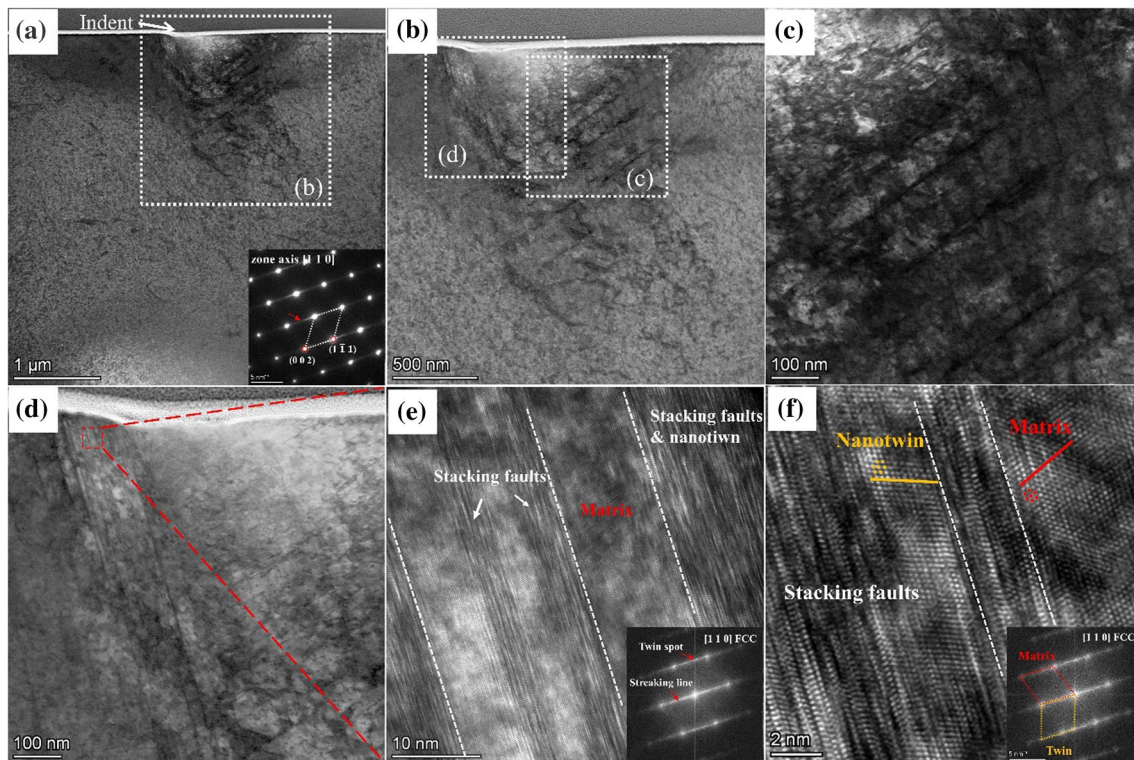


Fig. 5 **a** STEM bright-field image of the microstructure beneath the indent on the austenite grain with orientation of $[0\ 0\ 1]$ under maximum load of 3 mN. The lower right inset in **a** is the SADP with a zone-axis of $[1\ 1\ 0]$, red arrow indicates the streaking line feature. **b** The enlarged view of dashed rectangle area of **a**. **c** and **d** are the

magnified view of dashed rectangle inside **b**. **e** High-resolution TEM image (HRTEM) of red dashed area in **d**. **f** HRTEM image of another area close to indentation tip. The lower right insets of **e** and **f** are the fast Fourier transform (FFT) patterns, indicating the existence of stacking faults and deformation twins

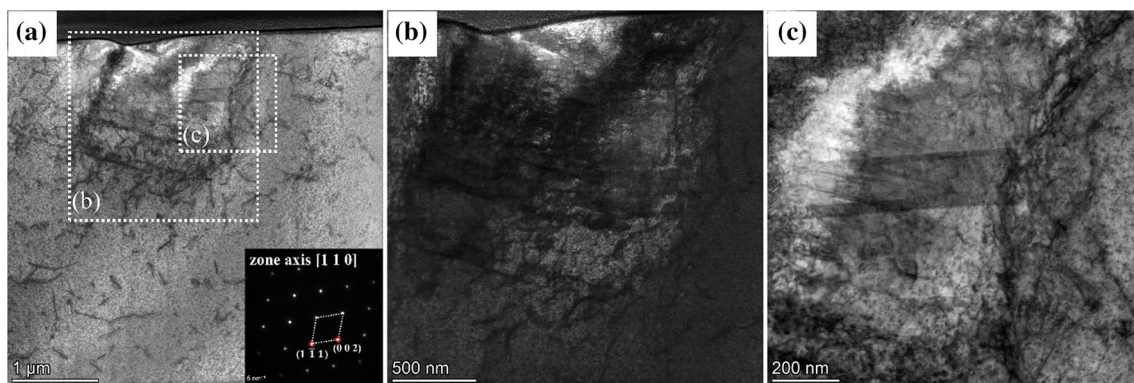


Fig. 6 **a** STEM bright-field image of the microstructure beneath the indent of austenite grain with orientation of $[1\ 1\ 1]$ under maximum load of 5 mN. The lower right inset in **a** is the SADP with a zone-axis of $[1\ 1\ 0]$. **b–c** Enlarged view of dashed rectangle area of **a**

cell under the maximum load of 5 mN is different from the randomly distributed dislocations in the indentation plastic zone with the maximum load of 3 mN (Fig. 4). Considering the similar orientation of indented austenite grain, the formation of dislocation cell could be due to the increase of the indentation load. The higher amount of dislocations generated at larger load has higher possibility to be trapped

by forest dislocations, which may rearrange to form a dislocation cell structure.

Figure 7 displays the microstructures under the nanoindentation of an austenite grain with normal direction of $[0\ 0\ 1]$ under a maximum load of 5 mN. The SADP indicates the formation of deformation twins and stacking faults (Fig. 7a). The dislocations expand to a depth over 2.5 μm , this is much

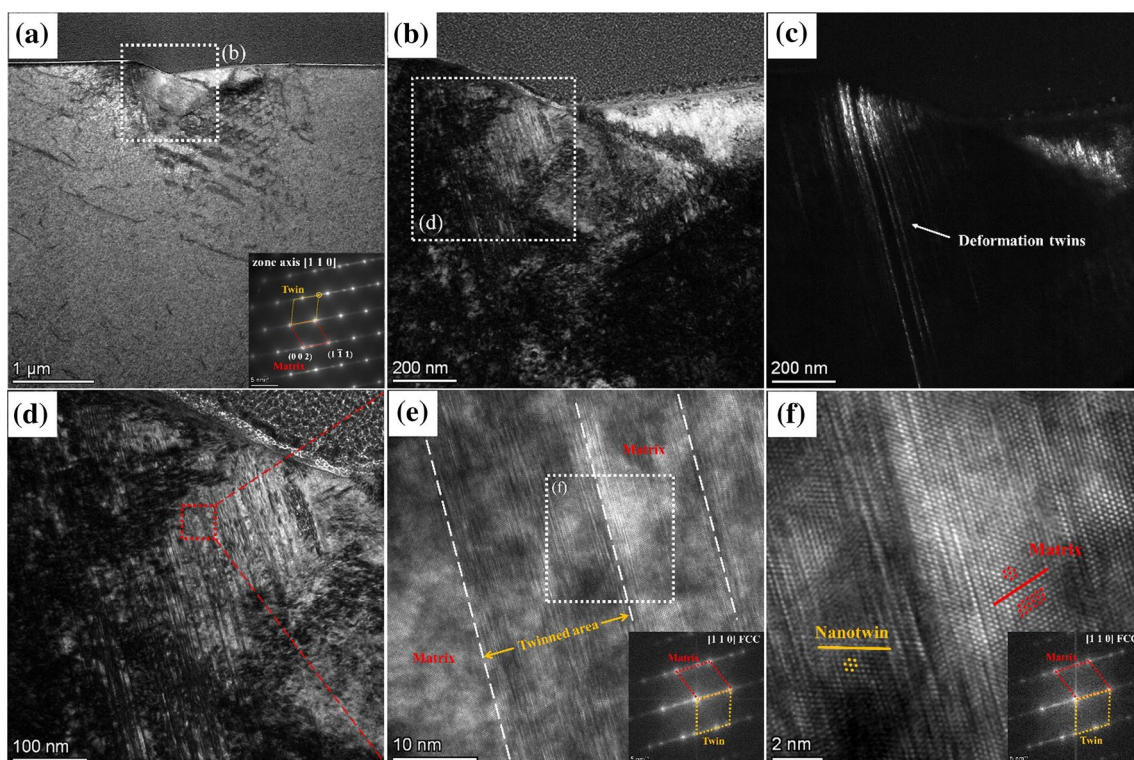


Fig. 7 **a** STEM bright-field image of the microstructure beneath the indent of austenite grain with orientation of $[0\ 0\ 1]$ under maximum load of 5 mN. The lower right inset in **a** is the SADP with a zone-axis of $[1\ 1\ 0]$. **b** Bright-field TEM image of the rectangle area in **a**. **c** The corresponding dark-field TEM image of **b**, indicating the for-

mation of deformation twins under indenter during nanoindentation. **d** The enlarged bright-field TEM image of the rectangle area in **b**. **e** HRTEM image of red dashed rectangle area in **d**. **f** The magnified view of rectangle area in **e**. Lower right insets in **e** and **f** are the corresponding FFT patterns

smaller than the travel distance (4 μm) of the dislocations in the $[1\ 1\ 1]$ -orientated grain (Fig. 6a). This reduced travel distance of dislocations in $[0\ 0\ 1]$ -orientated grain could be due to the formation of deformation twins, which impedes the glide of dislocations. The lamellar morphology (Fig. 7b) and the corresponding dark-field image (Fig. 7c) demonstrate the size and density deformation twins. Moreover, the magnified view of the deformation area around the indenter tip shows a mixture of stacking faults, deformation twins and dislocations (Fig. 7d). The detailed structure of these lamellas is revealed by high resolution TEM images (Fig. 7e, f), showing the presence of high-density stacking faults and deformation twins with incoherent boundary within the indentation plastic zone.

The present work investigates orientation dependent of twinning behavior in a typical twinning-induced plasticity steel during nanoindentation test. The specific orientations of the austenite grains selected for TEM observation are $[-25\ 36\ -17]$, $[-3\ 3\ 19]$, $[-9\ -8\ -9]$ and $[-4\ 6\ 25]$ based on EBSD measurement (Fig. 2). The corresponding Schmid factors for dislocation slip, leading and trailing Shockley partial dislocation glide associated with the primary slip systems are calculated and listed in Table 1. It is found that the

Table 1 Calculated Schmid factors for dislocation slip, leading and trailing Shockley partial dislocations glide along different directions under compression

| Axis | Slip system | Schmid factors | | |
|------------------|------------------------|----------------|-----------------|------------------|
| | | Slip | Leading partial | Trailing partial |
| $[1\ 1\ 1]$ | 6 equal systems | 0.272 | 0.157 | 0.314 |
| $[-25\ 36\ -17]$ | $(-1\ 1\ 1)[0\ 1\ -1]$ | 0.431 | 0.300 | 0.446 |
| $[-9\ -8\ -9]$ | $(1\ -1\ 1)[1\ 1\ 0]$ | 0.307 | 0.177 | 0.354 |
| $[0\ 0\ 1]$ | 8 equal systems | 0.408 | 0.471 | 0.235 |
| $[-3\ 3\ 19]$ | $(1\ 1\ 1)[-1\ 0\ 1]$ | 0.450 | 0.449 | 0.331 |
| $[-4\ 6\ 25]$ | $(1\ 1\ 1)[-1\ 0\ 1]$ | 0.472 | 0.451 | 0.366 |

austenite grains with orientation close to $[1\ 1\ 1]$ are free of deformation twins during nanoindentation test under a maximum load of 3 mN and 5 mN (Figs. 4 and 6). Nevertheless, the austenite grains with orientation close to $[0\ 0\ 1]$ demonstrate deformation twins beneath the indenter (Fig. 5). The orientation dependent deformation twinning behavior can

be ascribed to the different Schmid factors for the generation of partial dislocations. Only the orientations favorable for the generation of partial dislocations allow the nucleation of deformation twins [23, 35]. The [0 0 1]-orientated grains in this investigation have larger Schmid factor values for leading partial dislocation during compression, while the [1 1 1]-orientated grains have larger Schmid factor for trailing partial dislocations (Table 1). The twin nucleation is associated with the emission of leading partial dislocations on {111} planes [36]. A larger Schmid factor represents a higher stress on the leading partial during plastic deformation, which further promotes the nucleation of deformation twins. Accordingly, deformation twins are observed in the indentation plastic zone on the grains with orientations close to [0 0 1] (Figs. 5 and 7). In contrast, deformation twins are absent in grains with orientations close to [1 1 1] during deformation because of lower Schmid factor values for leading partial dislocations (Figs. 4 and 6).

Different from some micro-sized pillar compression investigations [22, 24, 37], the nucleation of deformation twin is more favored compared with twin growth during nanoindentation tests in the present study as the twin thickness is mostly less than 20 nm (Fig. 7). The deformation twins in micro-sized pillar are normally nucleated from the pillar surface by the emission of a few leading partial Shockley dislocations. The glide of three adjacent partial dislocations (or stacking faults) from the surface of micro-sized pillar into the pillar interior generates a deformation twin. The growth of twin is realized by emission of more leading partial dislocations on the adjacent {111} twinning planes with increase of strain. Note that the engineering strain in micro-sized pillar compression test is in the range of 6%–10% [24, 25], which is similar to the representative strain (8%) of nanoindentation test with a Berkovich indenter [38]. In other words, the deformation strain is not the main factor in affecting the twin thickness during pillar compression test or nanoindentation test. Compared with a micro-sized pillar compression test, there is only one free surface

for the emission of leading partial dislocations during the nanoindentation test. In contrast, the image force on the other side of pillar surface facilitates the slip of partial dislocations along twinning planes [30], making the growth of deformation twins favored during the pillar compression test.

Figure 8a is the SEM image of the present high Mn austenitic steel fabricated by cold rolling with a thickness reduction of 50% and subsequent recovery annealing at 500 °C for 15 min. The lamellar morphology within the austenite grains indicates the presence of deformation twin boundaries (Fig. 8a). The deformation twins are generated during the cold rolling process and are stable during the recovery annealing at 500 °C for 15 min [29]. Despite of the large cold reduction ratio (~50%), several austenite grains are still free of the deformation twins as marked by red arrows in Fig. 8a, which is also confirmed from the detailed EBSD measurement (Fig. 8b). The heterogeneous distribution of deformation twins in the austenite grains could be due to the effect of crystal orientation (i.e. Schmid factors) on the initiation of deformation twins as observed in the present nanoindentation investigation (Figs. 4, 5, 6 and 7). Therefore, the cold rolling process along single direction is insufficient to enable the decoration of deformation twins in all the austenite grains.

Recently, the effectiveness of dynamic Hall-Patch effect induced by formation of deformation twins in TWIP steel has been questioned from the observation that the contribution of deformation twins to the flow stress of TWIP steel is much lower than that of dislocations [13]. The present work suggests that the weak contribution of the deformation twins to the flow stress of TWIP steel shall also be due to the much less amount of deformation twins owing to the absence of deformation twins in certain crystal orientations. The orientation dependent deformation twinning behavior can also be found in tensile tested samples, where the austenite with certain orientations are free of deformation twins even after tensile to fracture [17]. Moreover, the cold rolling with thickness reduction of 50%

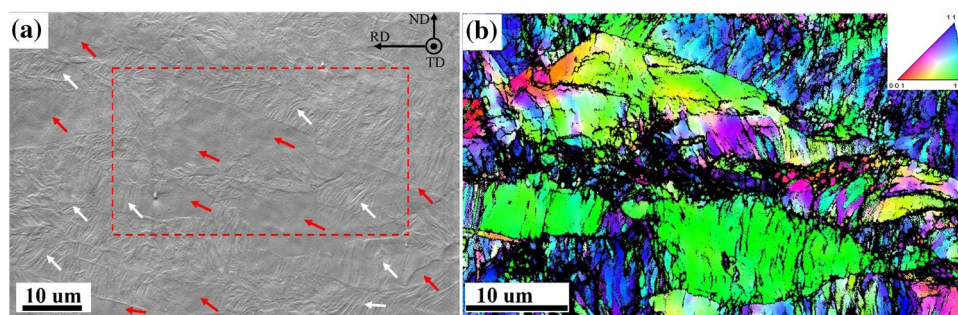


Fig. 8 **a** The SEM image of nanotwinned steel processed by cold rolling with thickness reduction of 50%, followed by recovery annealing at 500 °C for 15 min. The white arrows mark the austenite grains

with twin bundles and red arrows mark the grains free of twin bundles. **b** The corresponding EBSD orientation image of dashed rectangle area of **a**

along one direction is still ineffective to make the austenite grains with sufficient amount of deformation twin boundaries (Fig. 8). To strengthen the role of deformation twins to the flow stress, the present work suggests that the texture of TWIP steel should be properly controlled to maximize the amount of deformation twins during the plastic deformation [39]. The cold rolling along the different directions (i.e. cross rolling) may be useful to control the texture so that the amount of deformation twins can be maximized during the rolling process [40], which may increase the contribution of deformation twins to the flow stress of nanotwinned steel.

4 Conclusions

The present work investigates the effect of crystal orientation on the formation of deformation twins in TWIP steel by nanoindentation technique combined with detailed microstructural observation using EBSD and TEM. The conclusions are made as below.

1. The austenite grains with [0 0 1] orientation are favorable for the formation of deformation twins during nanoindentation test. In contrast, no deformation twins are observed in [1 1 1]-orientated austenite grains. The orientation dependent twinning behavior could be due to different Schmid factor values of the leading and trailing Shockley partial dislocations during compression.
2. Different from deformation twins, dislocations with high density can be found in either [0 0 1] or [1 1 1]-orientated austenite grains during nanoindentation test.
3. The dominated contribution of dislocations to the flow stress compared to that of deformation twins should also be related to crystal orientation, as the austenite grains with certain orientations are free of deformation twins. The present work suggests that the density of deformation twins could be enhanced by controlling crystal orientation through texture engineering or by deformation along different directions such as cross-rolling.

Acknowledgements B.B. He gratefully acknowledges the financial support from the National Natural Science Foundation of China (Grant No. U52071173) and Science and Technology Innovation Commission of Shenzhen (Project Nos. JCYJ20210324120209026, ZDSYS20200810171201007, KQTD2019092917250571). B.B. He would like to acknowledge the technical support from SUSTech Core Research Facilities.

Author Contribution X.K. Shang: Methodology, Investigation, Data curation, Formal analysis, Writing. S. Pan: Investigation. Q.W. Guan: Writing - review & editing. B.B. He: Review & editing, Funding acquisition.

Data Availability The raw data required to reproduce these findings are available from the corresponding author of this paper. The processed data required to reproduce these findings are available from the corresponding author of this paper.

Declarations

Conflict of interest The authors declared that they have no conflicts of interest to this work.

References

1. O. Bouaziz, H. Zurob, M. Huang, *Steel Res. Int.* **84**, 937 (2013)
2. B.B. He, B. Hu, H.W. Yen, G.J. Cheng, Z.K. Wang, H.W. Luo, M.X. Huang, *Science* **357**, 1029 (2017)
3. B.B. He, H.W. Luo, M.X. Huang, *Int. J. Plasticity* **78**, 173 (2016)
4. Z. Li, K.G. Pradeep, Y. Deng, D. Raabe, C.C. Tasan, *Nature* **534**, 227 (2016)
5. S. Allain, J.-P. Chateau, O. Bouaziz, S. Migot, N. Guelton, *Mater. Sci. Eng. A* **387–389**, 158 (2004)
6. A. Saeed-Akbari, J. Imlau, U. Prah, W. Bleck, *Metall. Mater. Trans. A* **40**, 3076 (2009)
7. B.C. De Cooman, in *Automotive Steels: Design, Metallurgy, Processing and Applications*, ed. by R. Rana, S.B. Singh (Woodhead Publishing, Sawston, 2017), pp. 317–385
8. B.C. De Cooman, Y. Estrin, S.K. Kim, *Acta Mater.* **142**, 283 (2018)
9. I. Gutierrez-Urrutia, D. Raabe, *Acta Mater.* **59**, 6449 (2011)
10. M.X. Huang, Z.Y. Liang, Z.C. Luo, *Mater. Sci. Technol.* **31**, 1265 (2015)
11. O. Bouaziz, N. Guelton, *Mater. Sci. Eng. A* **319–321**, 246 (2001)
12. O. Bouaziz, S. Allain, C. Scott, *Scripta Mater.* **58**, 484 (2008)
13. Z.Y. Liang, Y.Z. Li, M.X. Huang, *Scripta Mater.* **112**, 28 (2016)
14. L. Sun, X. He, J. Lu, *npj Comput. Mater.* **4**, 6 (2018)
15. Z.C. Luo, M.X. Huang, *Scripta Mater.* **142**, 28 (2018)
16. Z.C. Luo, M.X. Huang, *Scripta Mater.* **178**, 264 (2020)
17. H. Beladi, I.B. Timokhina, Y. Estrin, J. Kim, B.C. De Cooman, S.K. Kim, *Acta Mater.* **59**, 7787 (2011)
18. I. Gutierrez-Urrutia, D. Raabe, *Scripta Mater.* **66**, 992 (2012)
19. Z.Y. Liang, X. Wang, W. Huang, M.X. Huang, *Acta Mater.* **88**, 170 (2015)
20. K. Renard, H. Idrissi, D. Schryvers, P.J. Jacques, *Scripta Mater.* **66**, 966 (2012)
21. S. Curtze, V.-T. Kuokkala, *Acta Mater.* **58**, 5129 (2010)
22. S.Z. Wu, H.W. Yen, M.X. Huang, A.H.W. Ngan, *Scripta Mater.* **67**, 641 (2012)
23. W.S. Choi, B.C. De Cooman, S. Sandlöbes, D. Raabe, *Acta Mater.* **98**, 391 (2015)
24. W.S. Choi, S. Sandlöbes, N.V. Malyar, C. Kirchlechner, S. Korte-Kerzel, G. Dehm, B.C. De Cooman, D. Raabe, *Acta Mater.* **132**, 162 (2017)
25. Z.Y. Liang, J.T.M. De Hosson, M.X. Huang, *Acta Mater.* **129**, 1 (2017)
26. O. Kraft, P.A. Gruber, R. Mönig, D. Weygand, *Annu. Rev. Mater. Res.* **40**, 293 (2010)
27. W.C. Oliver, G.M. Pharr, *J. Mater. Res.* **7**, 1564 (1992)
28. E.J. Seo, J.K. Kim, L. Cho, J. Mola, C.Y. Oh, B.C. De Cooman, *Acta Mater.* **135**, 112 (2017)
29. P. Zhou, Z.Y. Liang, R.D. Liu, M.X. Huang, *Acta Mater.* **111**, 96 (2016)
30. D. Hull, D.J. Bacon, *Introduction to dislocations*, 5th edn. (Elsevier, Amsterdam, 2011)

31. E. Schmid, W. Boas, *Plasticity of Crystals with Special Reference to Metals* (F. A. Hughes & Co. Ltd., London, 1950)
32. K.L. Johnson, *Contact Mechanics* (Cambridge University Press, Cambridge, 1985)
33. S. Shim, H. Bei, E.P. George, G.M. Pharr, *Scripta Mater.* **59**, 1095 (2008)
34. L. Zhang, T. Ohmura, *Phys. Rev. Lett.* **112**, 145504 (2014)
35. I. Karaman, H. Sehitoglu, K. Gall, Y.I. Chumlyakov, H.J. Maier, *Acta Mater.* **48**, 1345 (2000)
36. Z.Y. Liang, M.X. Huang, *Metall. Mater. Trans. A* **52**, 5235 (2021)
37. Z.Y. Liang, M.X. Huang, *J. Mech. Phys. Solids* **85**, 128 (2015)
38. D. Tabor, *The Hardness of Metals* (Oxford University Press, Oxford, 2000)
39. S.H. Akbarian, A. Zarei-Hanzaki, A.S. Anoushe, H.R. Abedi, R. Unnikrishnan, G. Cios, *Mater. Sci. Eng. A* **799**, 140269 (2021)
40. Y. Jiang, X. Zhou, X.Y. Li, *Mater. Sci. Eng. A* **822**, 141703 (2021)

Publisher's Note Springer Nature remains neutral with regard to jurisdictional claims in published maps and institutional affiliations.